

# Polarization-Resolved Broad-Bandwidth Sum-Frequency Generation Spectroscopy of Monolayer Relaxation<sup>†</sup>

Marc Smits,<sup>\*,‡</sup> Maria Sovago,<sup>‡</sup> George W. H. Wurpel,<sup>‡</sup> Doseok Kim,<sup>§</sup> Michiel Müller,<sup>||</sup> and Mischa Bonn<sup>‡</sup>

FOM Institute for Atomic and Molecular Physics, Kruislaan 407, 1098 SJ, Amsterdam, The Netherlands, Department of Physics, Sogang University, Seoul, 121-742, Korea, and Swammerdam Institute for Life Sciences, University of Amsterdam, P.O. Box 94062, 1090 GB Amsterdam, The Netherlands

Received: November 10, 2006; In Final Form: January 5, 2007

A novel implementation of broad-bandwidth sum-frequency generation (SFG) spectroscopy is presented, which allows for the simultaneous recording of SFG spectra with different polarization combinations of the SFG, visible, and infrared beams. This method is particularly advantageous for studies in which surface properties are time-dependent, such as kinetic studies. The technique is illustrated by a study that mimics lung surfactant relaxation during the breathing cycle. The time-dependent molecular order of lung surfactant lipids is quantified through the vibrational response of the terminal CH<sub>3</sub> group.

## I. Introduction

Infrared–visible sum-frequency generation (SFG) is becoming an increasingly popular analytical tool in the study of surface molecular properties. As a surface-specific technique, it provides the surface vibrational spectrum which contains information about surface composition,<sup>1</sup> molecular conformation,<sup>2–5</sup> and molecular orientation,<sup>6–9</sup> without the need for labels, in a noninvasive manner. In SFG, an infrared (IR) beam and a visible (VIS) beam are combined at the surface to generate the SFG signal beam with a frequency which is the sum of the IR and VIS frequencies.<sup>10</sup> This process is forbidden in centrosymmetric media but is allowed at the surface where the symmetry is broken. When the frequency of the IR beam coincides with the resonance frequency of a vibrational transition, the SFG signal is significantly enhanced, providing the possibility to use SFG as a spectroscopic tool of surface vibrations. Using picosecond lasers, surface SFG spectra are collected by scanning the frequency of the IR laser. In broad-bandwidth or multiplex SFG,<sup>11,12</sup> the bandwidth of a femtosecond laser IR pulse is used to cover a  $\sim 200\text{ cm}^{-1}$  wide window of the vibrational spectrum. One advantage of this approach is that the sample response at all frequencies is recorded with every individual laser pulse and therefore all data points are recorded under identical conditions. This is unlike the case in picosecond mode where the IR-field is scanned and where the spectrum consists of as many different measurements (under potentially different conditions) as there are data points. This feature of broad-bandwidth SFG is particularly advantageous for the investigation of surfaces that may change in time, and it has been proven particularly useful for, for example, kinetic measurements (see, e.g., refs 13–17).

One of the enticing features of SFG is its capability to determine the orientation of specific molecular (sub) groups with respect to the surface plane by measuring the SFG intensity as

a function of the polarization of the different fields involved. Indeed, a promising application of SFG is to obtain the orientational information of lipids within a mono- or bilayer at the molecular level. This detailed knowledge is important to further understand the structure–function relationship of biomembranes. For instance, the outer leaflet of the plasma membrane of eukaryotic cells contains a significant amount of saturated phospholipids (mainly sphingomyelin), which are known to exhibit high affinity for cholesterol. Cholesterol is also present in large amounts ( $>25\text{ mol } \%$ ) in the plasma membrane and is known to have an ordering effect on the generally highly disordered lipids in the bilayer.<sup>18</sup> Polarization-resolved SFG can provide information on the induced ordering of lipids upon addition or extraction of cholesterol. Similarly, it would be interesting to investigate the influence of transmembrane spanning protein domains on the ordering of the lipids.

However, orientational information of surface molecules requires, in both implementations of SFG spectroscopy, the recording of at least two spectra under different polarization conditions (i.e., different measurements) of the incoming and emitted fields; in other words, it is still necessary to perform multiple experiments and to compare data that has not been measured under necessarily identical experimental conditions. Alternative techniques like the polarization null angle (PNA)<sup>19,20</sup> method to improve the accuracy of the determination of orientational parameters all suffer from the fact that data is obtained from different measurements. The advantage of (near) simultaneous determination of the different polarization contributions to the signal has been shown for various linear spectroscopic techniques like polarization modulation infrared reflection absorption spectroscopy<sup>21–23</sup> and T-format fluorescence anisotropy spectroscopy.<sup>24</sup>

In this paper, we present an extension of broad-bandwidth SFG, which enables the simultaneous measurement of two polarization combinations. This technique circumvents the problem of laser instabilities and changes in the sample over time and further facilitates the SFG measurements, in particular the determination of changes in molecular orientation when using SFG in kinetic mode.<sup>13–17</sup> We demonstrate the polariza-

<sup>†</sup> Part of the special issue “Kenneth B. Eisenthal Festschrift”.

\* To whom correspondence should be addressed. E-mail: smits@amolf.nl.

<sup>‡</sup> FOM Institute for Atomic and Molecular Physics.

<sup>§</sup> Sogang University.

<sup>||</sup> University of Amsterdam.

tion-resolved method by a kinetic study of lung surfactant compression and relaxation, which mimics the respiration cycle.<sup>25</sup> The main component of endogenous pulmonary surfactant in mammals is the lipid dipalmitoylphosphatidylcholine (DPPC). Its function is to lower the surface tension at the alveolar surface during exhalation, reducing the work required during the respiration cycle. Deficiency of the lung surfactant, particularly with premature infants, results in the (acute) respiratory distress syndrome. A recent study has investigated the collapse of DPPC monolayers by compressing the monolayer beyond its collapsing point.<sup>26,27</sup> Also, several studies on DPPC monolayers using SFG are available, mainly addressing the CH<sub>2</sub> and CH<sub>3</sub> groups in the chain<sup>28–30</sup> but also recently the CH<sub>2</sub> and CH<sub>3</sub> groups in the headgroup as well as the phosphate group.<sup>31</sup> In the study presented here, a monolayer of neat DPPC on a water subphase is compressed from low surface pressure to close to the collapsing point using a Langmuir trough, and subsequently the monolayer is decompressed and is allowed to relax. During the relaxation process, the molecular response is monitored in real-time through the spectral features of vibrational moieties within the molecule.

## II. Background

When two optical fields  $E_{\text{VIS}}$  and  $E_{\text{IR}}$  with frequency  $\omega_{\text{VIS}}$  and  $\omega_{\text{IR}}$ , respectively, are incident on an interface, a second-order nonlinear polarization  $P^{(2)}$  is induced that oscillates at the sum-frequency  $\omega_{\text{SFG}} = \omega_{\text{VIS}} + \omega_{\text{IR}}$

$$P_i^{(2)} = \chi_{ijk}^{(2)} E_{\text{VIS},j} E_{\text{IR},k} \quad (1)$$

Here,  $\chi_{ijk}^{(2)}$  represents the nonlinear susceptibility and  $i, j$ , and  $k$  represent one of the Cartesian coordinates  $x, y$ , or  $z$ . Using perturbation theory, the expression for  $\chi^{(2)}$  is obtained for the case when the IR field is (near-) resonant and the VIS beam is nonresonant.

$$\chi^{(2)} = A_0 e^{i\phi} + \sum_n \frac{A_n}{\omega - \omega_n + i\Gamma_n} \quad (2)$$

Here,  $A_0$  represents the nonresonant amplitude,  $\phi$  the relative phase,  $A_n$  the resonant amplitude,  $\omega$  the IR frequency,  $\omega_n$  the resonance frequency, and  $\Gamma_n$  the width of the resonance. The intensity  $I_{\text{SFG}}$  of the sum-frequency field that is emitted can be obtained using the nonlinear Fresnel factors  $L^{32}$

$$I_{\text{SFG}} \propto (L_i P_i^{(2)})^2 \quad (3)$$

For an isotropic surface, seven nonzero tensor elements exist. As a result, there are only four polarization combinations for which SFG is generated, namely, PPP, SPS, PSS, and SSP of, respectively, the SFG, VIS, and IR fields. By measuring SFG spectra at different polarization combinations, the (relative) values of the elements  $\chi_{ijk}^{(2)}$  can be obtained. Since the macroscopic nonlinear susceptibility tensor can be related to the molecular hyperpolarizability tensor, it is possible to obtain orientational information of a transition dipole moment and hence of a moiety of a surface molecule.<sup>33,34</sup> Since absolute values of the nonlinear susceptibility tensor can only be obtained when all experimental parameters are precisely known (including, e.g., detection efficiency), it is often more convenient to use relative values.

Our approach relies on the use of incident and generated fields polarized at 45°, in-between S- and P-polarized. Considering the possible polarization combinations, it is evident that, when one

TABLE 1: Overview of the Polarization Combinations

SFG (VI)	VIS	IR
P(PP) S(PS)	P	M=P/S
S(SP) P(SS)	S	
P(PP) S(SP)	M=P/S	P
S(PS) P(SS)		S

of the incident IR or VIS fields is polarized at 45° in-between S- and P-polarized (termed here “M-polarized”), SFG at both S and P polarization is emitted. As evident from Table 1, when  $E_{\text{IR}}$  is M-polarized, SFG can be generated in PPP- and SPS-mode, when  $E_{\text{VIS}}$  is P-polarized (and SSP and PSS when  $E_{\text{VIS}}$  is S-polarized). The same procedure can be applied when the VIS beam is M-polarized as is also indicated in Table 1.

As explained elsewhere,<sup>33,34</sup> by obtaining the ratio of the amplitudes of vibrations in different polarization combinations, the relative values of  $\chi^{(2)}$  can be obtained and the angle of the transition dipole moment of a vibrational moiety can be inferred. This method requires the reliable determination of the ratio of amplitudes obtained from two different spectra. When these spectra are recorded sequentially, the error in this ratio will be subject to systematic errors in, for example, polarization purities, but also to random errors, such as laser intensity fluctuations, time-dependent sample changes, and so forth. The contributions from many of the random errors vanish when using the polarization-resolved method presented here where the spectra are recorded simultaneously. Thus, this approach provides an inherently more reliable manner in which to determine molecular orientation at surfaces.

## III. Experiment

An overview of the experimental setup to measure polarization-resolved broad-bandwidth SFG spectra is depicted in Figure 1. Pulses centered at 800 nm of 1 mJ energy at 1 kHz repetition rate from a commercial femtosecond (pulse duration 100 fs) laser system (Coherent) were used to generate tunable mid-IR pulses in an optical parametric generator/optical parametric amplifier (TOPAS, Lightconversion) and of 0.5 mJ to generate the narrow band visible field centered at 800 nm (with a bandwidth of 5 cm<sup>-1</sup> using two etalons in series (with free spectral ranges of 9 and 25 nm, respectively)). For the experiments described here, the infrared field is centered at 2900 cm<sup>-1</sup> with a bandwidth of 200 cm<sup>-1</sup>. The IR frequency was set to probe simultaneously the CH<sub>3</sub> (and CH<sub>2</sub>) stretch vibrations in the sample. The polarization of both infrared and visible beams were controlled by polarizers and  $\lambda/2$ -plates, and the beams were focused onto the sample using  $f = 5$  cm and  $f = 30$  cm lenses, respectively. The beam diameters in the focus are approximately 100  $\mu\text{m}$ . The incident angles in the vertical plane are, respectively, 35° and 40° for the visible and infrared field.

The SFG signal is collected using an  $f = 10$ -cm lens and is analyzed using a beam-displacing prism (Melles Griot): the S-polarized light traverses unaffected, whereas the P-polarized light is displaced vertically by 4 mm. The SFG fields are spectrally dispersed using an imaging monochromator and are detected using an intensified charge-coupled device (iCCD) camera (PiMAXIII, Roper Scientific). The spectra of the two contributions with orthogonal polarization are recorded simul-

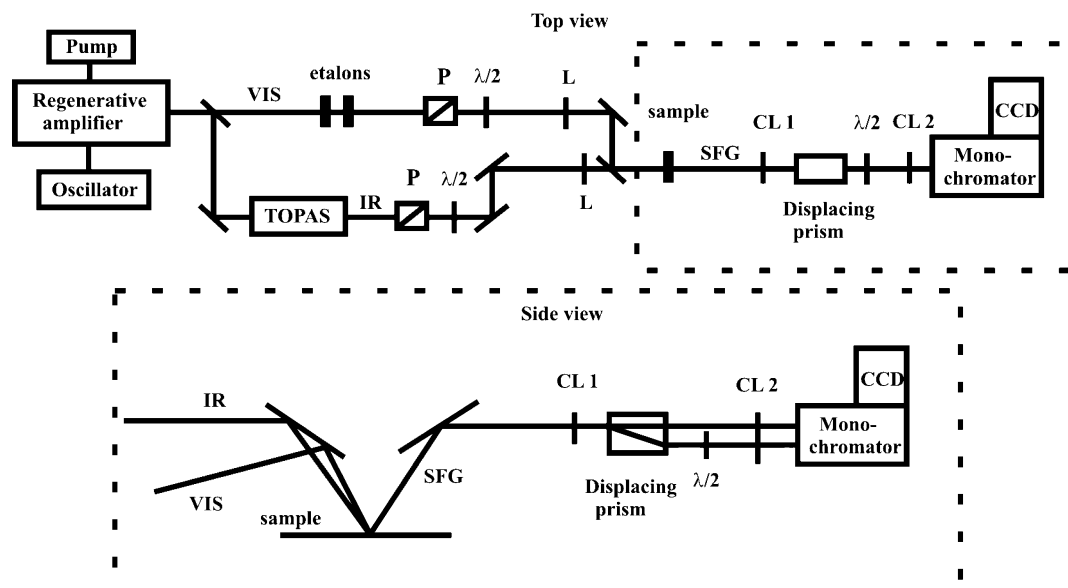


**Figure 1.** A schematic of the broad-bandwidth SFG setup. The output from the regenerative amplifier is split (BS1) into two: one part is used to pump an optical parametric amplifier (TOPAS) with a difference frequency unit to produce the broad-bandwidth IR-pulses; the other part is passed through two etalons to produce narrow-bandwidth VIS-pulses. The polarization of the two beams is cleaned up by polarizers (P) and can subsequently be rotated using  $\lambda/2$ -plates (VIS: M, IR: S or P). The two beams are focused with two lenses (L) onto the sample, and the signal beam is collected using a collimating lens. In the polarization-resolved method, the signal is focused in the horizontal plane by a cylindrical lens (CL1) and, depending on the polarization, is displaced by a polarizer prism. The P-polarized beam is rotated to S-polarization by an additional  $\lambda/2$ -plate for improved detection efficiency. Finally, the signal beams are focused onto the slit of the spectrometer using a second cylindrical lens (CL2). The residual visible (800-nm) light is filtered out using a short wave pass filter (SWP). The signal is spectrally analyzed using a monochromator, coupled to an iCCD camera. The bottom panel depicts a side view of the detection part of the setup.

taneously, imaged at different heights on the CCD camera. The P-polarized signal appears at the bottom of the CCD and the S-polarized signal appears at the top (see side view in Figure 1). Because of their collinear propagation from the sample point where the IR and VIS beams overlap, the two SFG beams cannot be simply focused onto the vertical entrance slit of the monochromator using a spherical lens, as they would be focused on the same spot. Instead, the light is focused onto the entrance slit in the horizontal plane using an  $f = 50$ -cm cylindrical lens in front of the beam-displacing prism and an  $f = 5$ -cm cylindrical lens in front of the entrance slit in the vertical plane. Additionally, having displaced the two beams in the vertical plane, it is simple to compensate for the different monochromator throughput and detection efficiency for S- and P-polarized light. We do so by simply adding a  $\lambda/2$ -plate to the lower of the two beams to convert the P-polarized signal beam into S-polarized, enhancing the detection efficiency in this channel by approximately a factor of 2. This also lifts the necessity for correcting for differences in detection efficiency for the two channels.

The sample used in this study consisted of a water (Millipore, 18.2 M $\Omega$  cm resistivity) subphase with a monolayer of DPPC (Avanti Polar Lipids, Birmingham, AL), initially at a surface pressure of 3.7 mN/m, that is, 75  $\text{\AA}^2$ /molecule. The monolayer was prepared in a commercial trough (Kibron Inc, Finland) by carefully spreading 0.5- $\mu\text{L}$  drops of 3.2 mM DPPC solution in chloroform (Sigma-Aldrich Chemical Co., St. Louis, MO). The surface pressure was monitored by a tensiometer using the Wilhelmy plate method. In Figure 2, the compression isotherm of DPPC, as well as a schematic representation of the Langmuir trough, is shown. The initial monolayer is in the liquid-expanded (LE) phase as indicated in Figure 2 with pressure  $\Pi_1$ . Next, the sample is compressed up to 35 mN/m ( $\Pi_2$  in Figure 2) in the liquid condensed (LC) phase and then is decompressed by gently but quickly moving the compression barrier to its original position. The moment the barrier has returned to its original position is defined as  $t = 0$ . The curved arrow in Figure 2

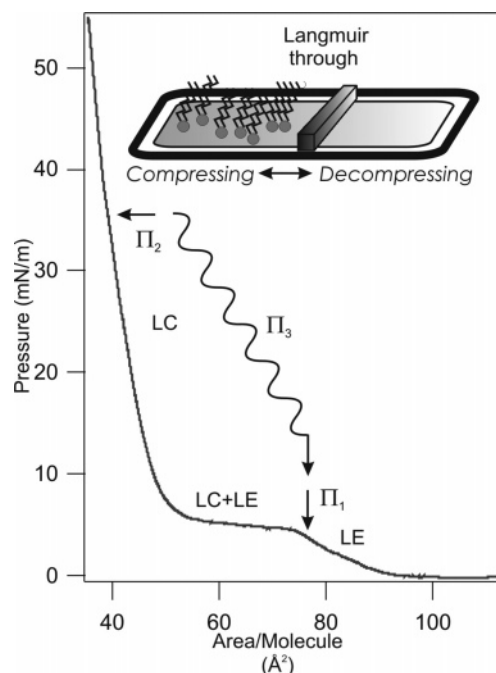


**Figure 2.** The isotherm of DPPC is shown as well as a schematic picture of the Langmuir trough. The initial pressure before compression is indicated as  $\Pi_1$ , the pressure to which the monolayer is compressed as  $\Pi_2$ , and the pressures during relaxation as  $\Pi_3$ .

indicates the time-dependent pressure  $\Pi_3$  during the relaxation process starting from pressure  $\Pi_2$  back to pressure  $\Pi_1$ .

The polarization-resolved broad-bandwidth SFG method relies on the generation of SFG with opposite polarization when one of the incoming beams is M-polarized. In the case of isotropic surfaces, it can be shown theoretically that indeed the two contributions to the SFG signal have opposite polarization, but in the general case for arbitrary symmetry, this is not necessarily

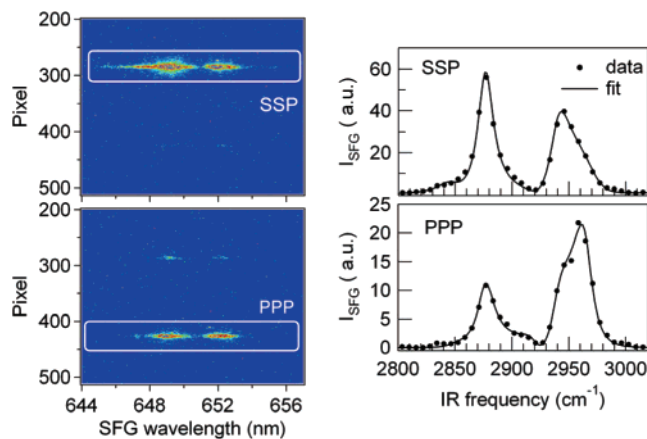


**Figure 3.** The raw CCD image recorded with S (top) and P (bottom) polarized VIS light is shown for a DPPC monolayer at “full” compression ( $\Pi_2 = 35$  mN/m). The presence of only one polarization component in each image indicates that the surface of the sample is isotropic. Next to the images, the corresponding spectra are shown (circles) by integrating the image in the vertical direction over the regions of interest as indicated. The solid line is a fit to the data.

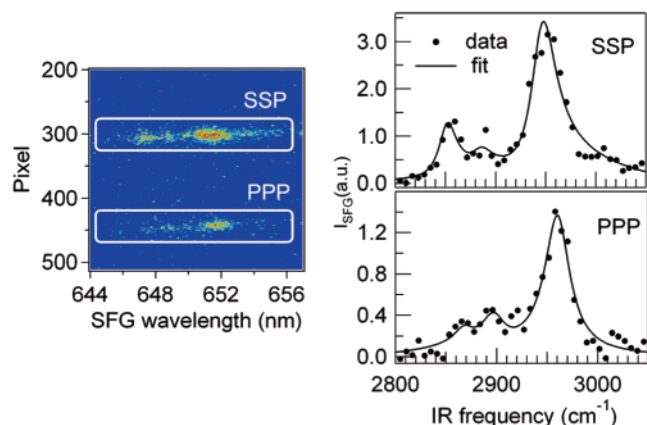


**Figure 4.** The raw image is shown for the polarizations SSP (top) and PPP (bottom), measured with the polarization-resolved method at a surface pressure  $\Pi_1 = 3.7$  mN/m. The signal appears at different vertical positions in the same CCD image because of the displacement prism. Next to the image, the corresponding spectra are shown (circles) by integrating the image in the vertical direction over the regions of interest as indicated. The solid line is a fit to the data.

true. It is well-known that DPPC forms an isotropic monolayer, but for completeness and as a demonstration of the approach presented here, it will be shown that the setup can be used to confirm the isotropic symmetry of the DPPC monolayer in a direct measurement. Hereto, the two polarization combinations are measured in the polarization-resolved setup, but in the conventional way, that is, with no M-polarized beams. If the surface is indeed isotropic, each polarization combination should result in an SFG beam of either S- or P-polarized light, but not both, that is, P-polarized IR and P-polarized VIS beams give rise to a P-polarized SFG beam and not S-polarized. Therefore, the full image recorded by the CCD camera should only contain one spectrum instead of two. In the left panel of Figure 3, the top image shows the SFG signal of a saturated DPPC monolayer, recorded with the VIS and IR polarized S and P, respectively (for an example of an image recorded with the VIS beam M-polarized, see Figure 4). In the top part of this image, the main signal is visible, corresponding to S-polarized SFG. The same is true for the VIS and IR polarized P, as shown in the bottom part of Figure 3, where the main signal is present in the lower part of the image corresponding to P-polarized SFG. This

clearly confirms that the surface is isotropic as anticipated. The small signals present at the bottom in the top image and the top of the bottom image are less than 10% of the main contribution. In principle, these signals could be due to a contribution from a non-isotropic surface (or chiral molecules), but additional measurements using gold as a reference indicate that these signals originate from slight impurities in the polarizations.

#### IV. Results

The kinetics of the monolayer relaxation are followed in real time by recording simultaneously the PPP and SSP spectra in the region of 2800–3100  $\text{cm}^{-1}$ . In Figure 4, the raw CCD image of the SFG signal from the monolayer before compression ( $\Pi_1$  in Figure 2) is displayed on the left. The acquisition time for this image, and for all images obtained during relaxation of the monolayer, is 20 s. The top part of the image in Figure 4 shows the SSP contributions of the SFG signal from the monolayer, whereas the bottom part shows the PPP contribution. On the right, the corresponding spectra are shown, obtained by vertical binning over the region of interest indicated in the image. The SFG spectrum of DPPC in this region is well-known from literature<sup>28–31</sup> and contains resonances from the symmetric  $\text{CH}_2$  stretch vibration at 2847  $\text{cm}^{-1}$  ( $\nu_{\text{s,CH}_2}$ ) the symmetric  $\text{CH}_3$  stretch vibration at 2870  $\text{cm}^{-1}$  ( $\nu_{\text{s,CH}_3}$ ), the antisymmetric  $\text{CH}_2$  stretch vibration at 2911  $\text{cm}^{-1}$  ( $\nu_{\text{as,CH}_2}$ ), the symmetric  $\text{CH}_2$  Fermi resonance ( $\nu_{\text{sFR,CH}_2}$ ) at 2893  $\text{cm}^{-1}$ , the symmetric  $\text{CH}_3$  Fermi resonance ( $\nu_{\text{sFR,CH}_3}$ ) at 2940  $\text{cm}^{-1}$ , and the antisymmetric  $\text{CH}_3$  stretch vibration at 2955  $\text{cm}^{-1}$  ( $\nu_{\text{as,CH}_3}$ ). The data from the relaxation process is fitted using eq 2 (solid line in Figure 4). Next, the monolayer is compressed up to 35 mN/m ( $\Pi_2$  in Figure 2) and is allowed to equilibrate. The time  $t = 0$  is defined as the return of the barrier to its original position. Immediately after the release of the barrier, the measurement is started, recording the two SFG spectra every 20 s for a total of 6 min. From the raw images, the SSP and PPP spectra are obtained (data not shown). All spectra are fitted using eq 2, where the peak positions and peak widths are fitted globally in all spectra. Because of the short acquisition time and the limited S/N, the peak areas in the region 2920–2980  $\text{cm}^{-1}$  are obtained as the most useful markers of the lipid order and orientation. In the SSP spectrum, the main component of this peak is the  $\nu_{\text{sFR,CH}_3}$ , whereas in the PPP spectrum the main component is the  $\nu_{\text{as,CH}_3}$ . In Figure 5, the normalized areas of these peaks are displayed as a function of time. The initial amplitudes at pressure  $\Pi_1$  are normalized to  $\pm 1$  to mark the opposite sign of the amplitudes of the  $\nu_{\text{sFR,CH}_3}$  and  $\nu_{\text{as,CH}_3}$  vibration. The temporal evolution of the surface pressure during the experiment is shown in the top panel of Figure 5. The different pressures as indicated in Figure 2 are added to the figure for convenience and the cartoons represent the morphology of the monolayer that will be used to discuss the time-dependent pressure during relaxation.

#### V. Discussion

Upon a change in surface lipid density, the surface pressure is a macroscopic indication of the relaxation process of the DPPC monolayer. After the release of the barrier, the pressure  $\Pi_3$  as indicated in Figure 2 shows a rapid decrease from pressure  $\Pi_2$  to a value below pressure  $\Pi_1$  (dashed line in the top panel of Figure 5), that is, an undershoot of the pressure. This behavior can be explained using the isotherm in Figure 2. After compression, the monolayer is in the LC phase as indicated in the first cartoon in Figure 5 as a dark area, that is, a homogeneous dense packing of lipid. When the barrier is

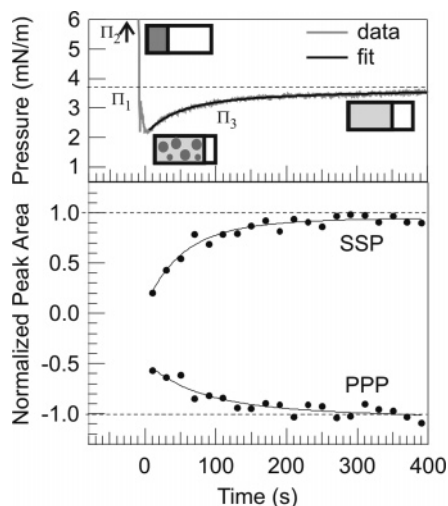


**Figure 5.** Normalized peak areas from the PPP and SSP spectrum are plotted as a function of time during the monolayer relaxation. The initial amplitudes are normalized to  $\pm 1$  (dashed line). The surface pressure during the relaxation process is shown in the top panel. The initial pressure  $\Pi_1$  is indicated as a dashed line. The cartoons are a representation of the monolayer morphology and show lipid domains (dark circular shapes) during the relaxation process.

removed, the monolayer falls apart in so-called domains (second cartoon in Figure 5 where the dark circular areas represent domains), and the monolayer contains both the LC and LE phase.<sup>35</sup> The average pressure in this coexistence region of the LC/LE phase can be lower than pressure  $\Pi_1$  because of the domain existence. The pressure is the average of the large area with low density of lipids and the small area of the domains with high density of lipids. Finally, the process of domain formation is followed by a much slower process where the domains disappear and the system eventually equilibrates to the original state: the lipids respread from the dense domains to eventually cover the whole surface evenly (third cartoon in Figure 5 with the light area to indicate low coverage). This slower process is seen in the top panel of Figure 5 as a recovery where the pressure approaches  $\Pi_1$  (dashed line). The slow component of the relaxation process can be described by a biexponential fit (solid line), with characteristic decay times of 60 and 300 s.

As a probe of the molecular changes during the relaxation process, the spectral features measured with the polarization-resolved broad-bandwidth SFG technique are used. In Figure 5, it can be seen that the changes in the peak areas (from 2920 to 2980  $\text{cm}^{-1}$ ) follow to some extent the surface pressure of the DPPC monolayer relaxation. The data is fitted using biexponential functions (solid lines) to obtain decay times of, respectively, 70/450 and 50/150 s for the PPP and SSP data. The decay is governed both by the change in the angle of the lipids and by the respreading of the lipids. Although no exact interpretation of the processes involved will be given, we attribute the second component partly to the respreading of the lipids. The first component we attribute to some extent to a change in molecular orientation as can be explained as follows: the main contribution to the peak areas arises from two perpendicular transition dipoles ( $\nu_{\text{as,CH}_3}$  and  $\nu_{\text{sFR,CH}_3}$ ) and thus a change in the ratio of the peak areas PPP/SSP can qualitatively be interpreted as an orientation change of the terminal  $\text{CH}_3$  group of the lipid chains. The computed ratio of the peak area is displayed as a function of time in Figure 6. The data shows one fast decay component that is fitted with a monoexponential function with a characteristic time of 15 s. This decay time is shorter than the components in the fit of the pressure. Therefore,

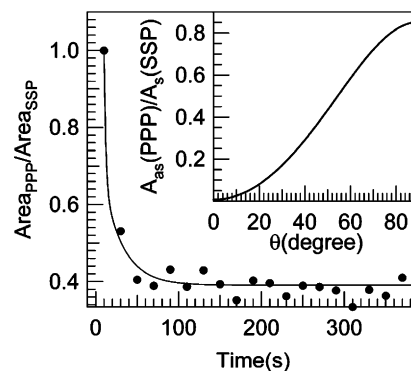


**Figure 6.** A relative orientation parameter is presented using the ratio of the peak area PPP/SSP. For qualitative comparison, the theoretical trend for the ratio of the  $\text{CH}_3$  vibrational amplitudes  $A_{\text{as}}(\text{PPP})/A_{\text{s}}(\text{SSP})$  is shown in the inset.

it can be concluded that only directly after the release of the barrier and the breakup of the continuous LC phase patches into domains will the angle of the chains readjust. During the remaining of the monolayer relaxation process, the angles of the chains remain unaffected, but the lipids respread according to the changes of the peak areas in Figure 5.

In principle, it is possible to obtain absolute angles for the average orientation of the terminal  $\text{CH}_3$  transition dipole from the data. In the inset of Figure 6, the theoretical ratio for the amplitudes of the antisymmetric  $\text{CH}_3$  vibration in the PPP spectrum ( $A_{\text{as,PPP}}$ ) and the symmetric  $\text{CH}_3$  vibration in the SSP spectrum ( $A_{\text{s,SSP}}$ ) is given as a function of the angle of the transition dipole of the  $\text{CH}_3$  group ( $\theta$ ). The amplitude of  $\nu_{\text{sFR,CH}_3}$  is assumed to follow the behavior of  $\nu_{\text{s,CH}_3}$ . The theoretical ratios are obtained using the method detailed elsewhere.<sup>33,34</sup> Briefly, the nonlinear Fresnel factors are computed and the different contributions of the relative  $\chi^{(2)}$  values to the PPP and SSP spectra are evaluated in case of the symmetric and asymmetric vibrations. The relevant parameters are the depolarization factor  $r = 2.3$ ,<sup>33</sup> the refractive index of air  $n_{\text{air}} = 1$ , the refractive index of the monolayer  $n_{\text{mono}} = 1.18$ , and the refractive index of water for, respectively, the SFG, VIS, and IR wavelength  $n_{\text{water}} = 1.331, 1.32 + 1.31i, \text{ and } 1.39 + 0.013i$ . The observed decrease of the peak area ratio PPP/SSP during the monolayer relaxation indicates that the vertical projection of the component of the dipole moment of the symmetric  $\text{CH}_3$  vibration increases. This is confirmed by the theoretical curve in the inset that shows an increase of  $\theta$  for larger ratios. Therefore, it can be concluded that while pressure increases directly after domain formation, on a molecular level, the lipid chains relax by reducing their tail angle with respect to the surface. Quantitative analysis using a global fit of the data yields a change in the angle of the chain from roughly  $90^\circ$  to  $70^\circ$ . The short acquisition time results in a large error in obtaining the amplitudes for the individual vibrations, resulting in a large uncertainty in the quantitative angle analysis. The error is increased further because of large uncertainty of the value for  $r$ , the errors introduced by the scaling of the  $\nu_{\text{sFR,CH}_3}$  to the  $\nu_{\text{s,CH}_3}$ , and the possible change in the distribution of the angles of the chains during relaxation.

Even though the error in the absolute angle is significant, the polarization-resolved method clearly shows the qualitative changes during the monolayer relaxation. Furthermore, it is shown that the extension of the broad-bandwidth SFG setup conveniently records the two polarization combinations simultaneously in a single measurement. This feature is particularly important in experiments where either sample instability or laser fluctuations cannot be avoided as, for example, shown in this kinetic study. More explicitly, the two spectra are recorded

simultaneously and therefore under exactly the same conditions. By measuring the kinetics of the monolayer relaxation in the polarization-resolved method as shown here, any fluctuations in either laser energy or sample composition will affect the two obtained spectra in the same manner. This effect can be observed in Figure 5, where the fluctuations in the amplitude of the CH<sub>3</sub> vibrations are clearly correlated. As a result, the S/N ratio in Figure 6, which shows the ratio of the two traces of Figure 5, is improved.

Finally, it is worth discussing four further improvements of the polarization-resolved technique that have not been exploited in this study: (1) in the polarization-resolved method, the angle of the M-polarized beam has to be set with high accuracy, that is, a 1° deviation leads to 10% more energy in either the P- or S-polarization. It is, however, more advantageous to set the angle for each sample such that roughly equal amounts of signal are detected in both polarization combinations. The angle can later be obtained very accurately from a reference signal from, for example, quartz. (2) In principle, the technique can be used with either  $E_{\text{IR}}$  or  $E_{\text{VIS}}$  to be M-polarized. In both situations, the two contributions to the SFG signal can be separated on the basis of the polarization of  $E_{\text{SFG}}$ . When all three polarization combinations have to be obtained, two independent measurements are still required. By choosing  $E_{\text{IR}}$  instead of  $E_{\text{VIS}}$  to be M-polarized, the SPS and PSS spectra are measured in two sequential measurements. These two spectra are, however, identical in case of a nonresonant VIS beam (apart from a scaling factor). In this way, two sets with each two spectra are obtained. The spectra within the first set are measured simultaneously and can be compared directly. The second set contains one spectrum that is equivalent to a spectrum of the first set and can be used to scale the second data set for comparison with the first data set. For the situation where the  $E_{\text{VIS}}$  is M-polarized, the two equivalent spectra end up in the same data set and hence comparison with the other data set is obscured. (3) The data from kinetic measurements can be improved further by combining the polarization-resolved method with time-correlated techniques. The latter approach has been shown for the dilatational properties of DPPC monolayers using the pressure response as a function of the frequency of a sinusoidal variation (with period  $T$ ) in surface area.<sup>36</sup> By averaging spectra recorded at different times with fixed intervals  $T$ , the noise in the data presented here can, in principle, be further reduced. (4) If the impurities in the polarization of the VIS and IR beams can be neglected and the separation of the polarization components of the signal is sufficient, the polarization-resolved technique can be used for chiral surfaces to obtain simultaneously the “normal” and chiral components of the signal.<sup>37</sup> Hereto, the setup is used in the traditional scheme with pure polarizations. Choosing the polarization of the VIS and IR beam, respectively, S and P, the normal SFG signal SSP and the chiral signal PSP are measured simultaneously.

## VI. Conclusions

To conclude, we have presented a novel implementation of broad-bandwidth SFG, which allows for the simultaneous recording of spectra with different polarization. Such spectra are required to obtain orientational information of surface molecules. The approach circumvents possible problems related to fluctuations in the signal because of instability of the laser or changes of the sample in time and should be especially useful for kinetic studies, allowing for an increased accuracy in determining orientational parameters. The only additional optics required for this technique are two cylindrical lenses, a beam-displacing prism and optionally a  $\lambda/2$  plate.

**Acknowledgment.** This work is part of the research program of the Stichting Fundamenteel Onderzoek der Materie (Foundation for Fundamental Research on Matter) with financial support from the Nederlandse Organisatie voor Wetenschappelijk Onderzoek (Netherlands Organization for the Advancement of Research). M.S. and M.S. contributed equally to this work.

## References and Notes

- Bain, C. D.; Davies, P. B.; Ong, T. H.; Ward, R. N.; Brown, M. A. *Langmuir* **1991**, *7*, 1563.
- Miranda, P. B.; Pflumio, V.; Saijo, H.; Shen, Y. R. *Chem. Phys. Lett.* **1997**, *264*, 387.
- Conboy, J. C.; Messmer, M. C.; Richmond, G. L. *J. Phys. Chem.* **1996**, *100*, 7617.
- Chen, X. Y.; Clarke, M. L.; Wang, J.; Chen, Z. *Int. J. Mod. Phys. B* **2005**, *19*, 691.
- Kataoka, S.; Cremer, P. S. *J. Am. Chem. Soc.* **2006**, *128*, 5516.
- Zhang, D.; Gutow, J.; Eisenthal, K. B. *J. Phys. Chem.* **1994**, *98*, 13729.
- Rao, Y.; Comstock, M.; Eisenthal, K. B. *J. Phys. Chem. B* **2006**, *110*, 1727.
- Sass, M.; Lettenberger, M.; Laubereau, A. *Chem. Phys. Lett.* **2002**, *356*, 284.
- Chen, K. B.; Chang, C. H.; Yang, Y. M.; Maa, J. R. *Colloids Surf., A* **2003**, *216*, 45.
- Shen, Y. R. *Nature* **1989**, *337*, 519.
- Richter, L. J.; Petralli-Mallow, T. P.; Stephenson, J. C. *Opt. Lett.* **1998**, *23*, 1594.
- Ham, E. W. M. v. d.; Vreken, Q. H. F.; Eliel, E. R. *Opt. Lett.* **1996**, *21*, 1448.
- Rasing, T.; Stehlin, T.; Shen, Y. R.; Kim, M. W.; Valint, P. *J. Chem. Phys.* **1988**, *89*, 3386.
- Roeterdink, W. G.; Berg, O.; Bonn, M. *J. Chem. Phys.* **2004**, *121*, 10174.
- Westerberg, S.; Wang, C.; Somorjai, G. A. *Surf. Sci.* **2005**, *582*, 137.
- Hobel, F.; Bandara, A.; Ruppel, G.; Freund, H. J. *Surf. Sci.* **2006**, *600*, 963.
- Liu, J.; Conboy, J. C. *Biophys. J.* **2005**, *89*, 2522.
- Gennis, R. B. *Biomembranes. Molecular structure and function*; Springer-Verlag Inc.: New York, 1989.
- Chen, H.; Gan, W.; Wu, B. D.; Wu, Z. Z.; Wang, H. *Chem. Phys. Lett.* **2005**, *408*, 284.
- Wang, J.; Chen, X. Y.; Clarke, M. L.; Chen, Z. *Proc. Natl. Acad. Sci. U.S.A.* **2005**, *102*, 4978.
- Estrela-Lopis, I.; Brezesinski, G.; Mohwald, H. *Biophys. J.* **2001**, *80*, 749.
- Buffeteau, T.; Desbat, B.; Turlet, J. M. *J. Appl. Spectrosc.* **1991**, *45*, 380.
- Itoh, K.; Oguri, H. *Langmuir* **2006**, *22*, 9208.
- Lakowicz, J. R. *Principles of fluorescence spectroscopy*; Kluwer Academic: New York, 1999.
- Goerke, J. *Biochim. Biophys. Acta* **1998**, *1408*, 79.
- Gopal, A.; Lee, K. Y. C. *J. Phys. Chem. B* **2006**, *110*, 22079.
- Chen, K. B.; Chang, C. H.; Yang, Y. M.; Maa, J. R. *Colloids Surf., A* **2003**, *216*, 45.
- Bonn, M.; Roke, S.; Berg, O.; Juurlink, L. B. F.; Stamouli, A.; Muller, M. *J. Phys. Chem. B* **2004**, *108*, 19083.
- Roke, S.; Schins, J.; Muller, M.; Bonn, M. *Phys. Rev. Lett.* **2003**, *90*, 128101.
- Watry, M. R.; Tarbuck, T. L.; Richmond, G. I. *J. Phys. Chem. B* **2003**, *107*, 512.
- Ma, G.; Allen, H. C. *Langmuir* **2006**, *22*, 5341.
- Shen, Y. R. *Frontiers in Laser Spectroscopy*, Proceedings of the International School of Physics “Enrico Fermi”, Course CXX, June 23–July 3, 1992; North-Holland: Amsterdam, 1994.
- Zhuang, X.; Miranda, P. B.; Kim, D.; Shen, Y. R. *Phys. Rev. B* **1999**, *59*, 12632.
- Wang, H. F.; Gan, W.; Lu, R.; Rao, Y.; Wu, B. H. *Int. Rev. Phys. Chem.* **2005**, *24*, 191.
- Hu, Y. F.; Meleson, K.; Israelachvili, J. *Biophys. J.* **2006**, *91*, 444.
- Saulnier, P.; Boury, F.; Malzert, A.; Heurtault, B.; Ivanova, Tz.; Cagna, A.; Panaïotov, I.; Proust, J. E. *Langmuir* **2001**, *17*, 8104.
- Ji, N.; Ostroverkhov, V.; Belkin, M.; Shiu, Y. J.; Shen, Y. R. *J. Am. Chem. Soc.* **2006**, *128*, 8845.